Adsorption of HgO on the Au(111) Surface: A Dual Machine-Learning Force-Field Benchmark with Epistemic Uncertainty Quantification, Thermodynamic Analysis, and Surface Diffusion Characterization

Hossam Mohamed[1,*]
Dipayan Sen[2,†]

[1]Faculty of Science, Aswan University, Aswan, Egypt
[2]Joint Institute for Nuclear Research (JINR)

[*]Corresponding author: hossam.magdy@stu.sci.aswu.edu.eg
[†]Supervisor

April 17, 2026

Abstract

Mercury contamination of the atmosphere and aquatic ecosystems constitutes one of the most pressing environmental challenges of the twenty-first century, motivating intensive research into solid-state sorbents capable of capturing mercury oxide (HgO) under realistic conditions. Gold surfaces, owing to the exceptionally strong affinity between gold and mercury, represent a promising platform for such capture. However, the computational cost of density functional theory (DFT) has historically prevented systematic exploration of molecular adsorption, tilt-angle dependence, uncertainty quantification, and finite-temperature dynamics on realistic slab models. Here we address this gap by deploying two state-of-the-art machine learning force fields (MLFFs)—CHGNet v0.3.0 (412 525 parameters) and MACE-MP-0 (large variant)—to study HgO adsorption across all four high-symmetry sites of the Au(111) surface. Using a $4 \times 4 \times 5$ slab model with 20 Å vacuum, we determine adsorption energies of $-1.9768\,\mathrm{eV}$ (ontop), $-2.0423\,\mathrm{eV}$ (bridge), $-1.9673\,\mathrm{eV}$ (fcc), and $-2.0086\,\mathrm{eV}$ (hcp), establishing the bridge site as the thermodynamically preferred binding location. Epistemic uncertainty quantification via weight-perturbation ensembles ($N = 5$, $\sigma_w = 0.001$) yields $\sigma_{\mathrm{UQ}} \approx 216\,\mathrm{meV}$ for all CHGNet sites, dominated by slab energy fluctuations ($\sigma_{\mathrm{slab}} = 149.3\,\mathrm{meV}$). Critically, all inter-site signal-to-noise ratios fall below unity, revealing that site discrimination at the current MLFF level is limited by epistemic uncertainty. Cross-model validation shows quantitative agreement at hollow sites but a 601 meV discrepancy at the ontop geometry; MACE-MP-0 fails structurally at 45° tilt configurations, producing unphysical Hg–O bond elongations of 2.98–3.67 Å. Vibrational analysis uncovers systematic frequency softening with scale factors of 1.58–1.90, while scaled zero-point energy corrections of

260–307 meV are non-negligible. Langevin molecular dynamics at 300 K and 500 K reveals surface diffusion coefficients of $6.51 \times 10^{-19}\,\mathrm{cm}^2\,\mathrm{s}^{-1}$ and $1.25 \times 10^{-18}\,\mathrm{cm}^2\,\mathrm{s}^{-1}$, respectively, with a bond-breaking event occurring at $t \approx 1.12\,\mathrm{ps}$ at 500 K. Free energy surface analysis from MD trajectories maps the landscape of surface migration, confirming sub-angstrom localization at 300 K. Free energy calculations confirm thermodynamic irreversibility across 200–900 K. Coverage studies reveal attractive lateral interactions (-248–-611 meV/molecule), suggesting cooperative binding and potential for high-capacity mercury capture. These results establish a comprehensive MLFF benchmark for heavy-metal-oxide adsorption on noble metal surfaces and highlight key limitations requiring DFT validation.

Contents

1 Introduction

Mercury is a persistent global pollutant whose environmental toxicity has been recognized since the Minamata disaster of the 1950s and is now subject to international regulatory frameworks including the Minamata Convention [1]. In the atmosphere, mercury cycles through elemental (Hg^0), oxidized (Hg^{2+}), and particle-bound forms, with mercury oxide (HgO) representing a key oxidized species formed through reactions with atmospheric oxidants [2]. Anthropogenic point sources—coal combustion, chlor-alkali plants, and non-ferrous metal smelting—emit substantial quantities of mercury annually [21], necessitating efficient capture technologies that can operate at realistic temperatures.

Gold-based sorbents have attracted considerable attention for mercury capture owing to the remarkably strong affinity between gold and mercury, which underpins the ancient technique of amalgamation and modern sensor applications [4, 5]. The Au(111) surface, being the lowest-energy facet of face-centred cubic gold, serves as the canonical model for computational and experimental investigations of heavy-metal interactions, including as a benchmark system for probing the stability of superheavy elements such as copernicium (Cn), nihonium (Nh), and flerovium (Fl) on metallic substrates [6, 3]. Previous DFT investigations of Hg and Hg^0 on Au(111) have established binding energies in the range of -0.5–-1.2 eV [5], but the adsorption of the oxidized species HgO—relevant to atmospheric chemistry and industrial off-gas treatment—has received considerably less attention, particularly with respect to tilt-angle-dependent binding, finite-temperature stability, and lateral interactions at non-zero coverage.

The computational challenge is significant. High-accuracy DFT calculations for a $4 \times 4 \times 5$ Au(111) slab with an adsorbate require on the order of 10^4–10^5 self-consistent field iterations per geometry step, making systematic exploration of configuration space, uncertainty quantification, and molecular dynamics trajectories computationally prohibitive at the DFT level. Machine learning force fields offer a transformative solution to this bottleneck [7]. By training universal interatomic potentials on large databases of DFT calculations spanning a wide range of chemical environments, models such as CHGNet [8] and MACE-MP-0 [9] can achieve near-DFT accuracy at a fraction of the computational cost, enabling calculations that were previously inaccessible.

CHGNet (Crystal Hamiltonian Graph neural NETwork) is a graph neural network potential trained on the Materials Project trajectory database, incorporating charge, spin, and structural degrees of freedom through a sophisticated message-passing architecture with 412 525 learnable parameters [8]. MACE-MP-0 employs equivariant message-passing networks based on $E(3)$-equivariant representations (MACE framework), providing rotationally covariant force predictions with high data efficiency [9, 16]. Both models are universal potentials capable of treating the full periodic table, making them immediately applicable to the Au–Hg–O ternary system without additional fine-tuning.

A critical and underappreciated challenge in MLFF-based adsorption studies is epistemic uncertainty—the inherent uncertainty in model predictions arising from limited training data coverage and model architecture choices. For site-selective adsorption, where energy differences between binding sites may be as small as tens of meV, the question of whether the MLFF can reliably distinguish between sites is non-trivial and seldom addressed [15]. The signal-to-noise ratio between inter-site energy differences and model uncertainty constitutes a figure of merit for MLFF reliability in this context.

In this work, we present a complete computational benchmark study of HgO adsorption on Au(111) using CHGNet v0.3.0 and MACE-MP-0, encompassing: (i) geometry optimization at all four high-symmetry sites with systematic tilt-angle exploration; (ii) epistemic uncertainty quantification via weight-perturbation ensembles with Gaussian error propagation; (iii) statistical sampling of the local energy landscape; (iv) vibrational analysis with experimental frequency scaling; (v) finite-temperature free energy calculations spanning 200–900 K; (vi) Langevin molecular dynamics at 300 K and 500 K with free energy surface mapping; (vii) global potential energy surface mapping; (viii) bond activation and coordination number analysis; and (ix) multi-molecule coverage effects up to four adsorbates. Throughout, we report complete provenance for all 65 calculated quantities and discuss the 5 failed calculations as physically meaningful results.

2 Computational Methods

2.1 Slab Model Construction

The Au(111) surface was modelled using a $4 \times 4 \times 5$ supercell containing 80 Au atoms, constructed with the Atomic Simulation Environment (ASE) [10] using the `fcc111` function. The experimental lattice constant $a = 4.0780$ Å (Wyckoff 1963 [14]) was adopted for slab construction. A vacuum layer of 20 Å was applied perpendicular to the surface to eliminate spurious periodic interactions. The bottom two layers of the slab were fixed at their bulk positions using ASE's `FixAtoms` constraint, while the upper three layers and any adsorbates were permitted to relax. Four high-symmetry adsorption sites were considered: ontop, bridge, fcc hollow, and hcp hollow. For each site, the HgO molecule was placed with the O atom at height $h = 2.5$ Å above the surface and two initial tilt angles tested: 0 and 45.

We note that a Materials Project API query for structure `mp-81` returned $a = 2.9495$ Å, which is inconsistent with the known fcc structure of bulk gold (expected $a \approx 4.08$ Å) and was rejected as likely corresponding to a BCC polymorph or an API indexing artefact; the experimental value was used instead.

2.2 Machine Learning Force Fields

CHGNet v0.3.0 was loaded via the `chgnet` Python package with 412 525 trainable parameters, deployed on GPU (CUDA) in `float32` precision via the ASE-compatible `CHGNetCalculator` interface. **MACE-MP-0** (large variant) was loaded via the `mace-torch` package using Materials Project pretrained weights, run in `float64` precision as recommended for geometry optimization. Both models were used directly from their pretrained weights with no system-specific fine-tuning.

2.3 Geometry Optimization

All structural relaxations employed the FIRE optimizer [12] as implemented in ASE, with $F_{\text{max}} = 0.01$ eV/Å and a maximum of 500 steps. The adsorption energy was defined as:

$$E_{\text{ads}} = E_{\text{slab+mol}} - E_{\text{slab}} - E_{\text{HgO}} \tag{1}$$

Physical validity was enforced through automated assertion checks: $-5.0 < E_{\text{ads}} < -0.05$ eV, $1.8 < d(\text{Hg} - \text{O}) < 2.5$ Å, and a minimum bond change of 0.001 Å relative to gas-phase geometry.

2.4 Uncertainty Quantification

Epistemic uncertainty was estimated via a weight-perturbation ensemble approach. For each MLFF, $N = 5$ perturbed copies were generated by adding Gaussian noise $\mathcal{N}(0, \sigma_w^2)$ with $\sigma_w = 0.001$ to all model parameters. The total uncertainty on the adsorption energy was propagated in quadrature:

$$\sigma_{\mathrm{UQ}} = \sqrt{\sigma_{\mathrm{ads}}^2 + \sigma_{\mathrm{slab}}^2 + \sigma_{\mathrm{HgO}}^2} \tag{2}$$

The inter-site signal-to-noise ratio for sites i and j was:

$$\mathrm{SNR}_{ij} = \frac{|E_{\mathrm{ads},i} - E_{\mathrm{ads},j}|}{\sqrt{\sigma_{\mathrm{UQ},i}^2 + \sigma_{\mathrm{UQ},j}^2}} \tag{3}$$

with SNR ≥ 1.0 adopted as the threshold for statistically resolved site discrimination.

2.5 Statistical Sampling

For the two most stable CHGNet sites (bridge and hcp), $N = 20$ independent geometry optimizations were performed from structurally perturbed initial conditions ($\sigma_{\mathrm{noise}} = 0.10\,\text{Å}$). The resulting ensemble of adsorption energies was analysed using Gaussian mixture models (GMM) with Bayesian information criterion (BIC) selection to identify energy basins.

2.6 Vibrational Analysis

Vibrational frequencies were computed using the finite-difference `Vibrations` module in ASE (displacement $0.01\,\text{Å}$). The frequency scale factor was defined as $\mathrm{SF} = \nu_{\mathrm{exp}}/\nu_{\mathrm{raw}}$ where $\nu_{\mathrm{exp}} = 740.0\,\mathrm{cm}^{-1}$ [13]. Scaled ZPE corrections were computed as $\mathrm{ZPE}_{\mathrm{scaled}} = \frac{1}{2}\sum_i hc\nu_i^{\mathrm{scaled}}$.

2.7 Thermodynamics

The adsorption free energy $\Delta G(T)$ combined translational entropy via the Sackur–Tetrode equation, rigid-rotor rotational entropy of linear HgO, and harmonic oscillator vibrational free energies:

$$\Delta G(T) = E_{\mathrm{ads}} + \left[F_{\mathrm{vib,ads}}(T) - F_{\mathrm{vib,gas}}(T)\right] - F_{\mathrm{trans}}(T) - F_{\mathrm{rot}}(T) \tag{4}$$

Calculations spanned $T = 200 - -900\,\mathrm{K}$ at standard pressure.

2.8 Molecular Dynamics and Free Energy Surface

Langevin NVT molecular dynamics was performed using ASE's `Langevin` integrator ($\Delta t = 1.0\,\mathrm{fs}$, $\gamma = 0.02\,\mathrm{fs}^{-1}$, 2000 steps) at 300 K and 500 K for the bridge site, and 300 K for the hcp site. The surface diffusion coefficient was extracted as $D = \mathrm{slope}/4$ from linear regression of the second half of the MSD trajectory. The two-dimensional free energy surface (2D-FES) was constructed from the oxygen atom trajectory using:

$$G(x, y) = -k_{\mathrm{B}}T \ln P(x, y) \tag{5}$$

where $P(x, y)$ is the 2D probability density from a 40×40 histogram of lateral displacements, smoothed with a Gaussian kernel ($\sigma = 1$ bin). A one-dimensional free energy profile was extracted via principal component analysis (PCA) of the trajectory, projecting onto the dominant diffusion direction.

2.9 Potential Energy Surface Mapping and Coverage Effects

A global PES survey was performed on a 12×12 grid spanning one surface unit cell at fixed O height $h = 2.05$ Å (single-point, no relaxation). Multi-molecule adsorption studies were conducted for $N = 1$, 2, and 4 HgO molecules, with the lateral interaction energy per molecule defined as $E_{\text{lat}} = E_{\text{ads}}^{(N)} - E_{\text{ads}}^{(1)}$.

3 Results and Discussion

3.1 Reference Molecule and Slab Validation

Before undertaking adsorption calculations, we validated the MLFF predictions against available experimental benchmarks. CHGNet predicts an Hg–O bond length of $d_{\text{CHGNet}} = 1.9788$ Å and total energy of -3.7047 eV for the isolated molecule. MACE-MP-0 gives $d_{\text{MACE}} = 2.1538$ Å and -2.8944 eV. The experimental Hg–O bond length in gaseous HgO is 2.0560 Å [13]. CHGNet thus underestimates the bond length by 0.077 Å (-3.7%) while MACE overestimates by 0.098 Å ($+4.8\%$).

The HgO stretching frequency provides a more sensitive diagnostic. CHGNet yields $\nu_{\text{CHGNet}} = 495.8\,\text{cm}^{-1}$ and MACE gives $\nu_{\text{MACE}} = 307.2\,\text{cm}^{-1}$, both substantially below the experimental value of $740.0\,\text{cm}^{-1}$ [13]. These systematic underestimates reflect the soft treatment of the Hg–O bond potential by both MLFFs and necessitate the application of frequency scaling factors in all subsequent vibrational analysis (Section 3.6). The Au slab energies were -253.7983 eV (CHGNet) and -253.7994 eV (MACE) for the 80-atom slab, consistent with DFT-PBE estimates for bulk gold [11].

3.2 Cross-Model Validation

Figure 1 presents the cross-model validation of adsorption energies and epistemic uncertainties between CHGNet and MACE-MP-0.

The two MLFFs agree at the fcc (-2.0168 eV MACE vs. -1.9673 eV CHGNet, difference 50 meV) and hcp sites (-1.9283 eV MACE vs. -2.0086 eV CHGNet, difference 80 meV), but diverge substantially at ontop (-1.3762 eV MACE vs. -1.9768 eV CHGNet, difference 601 meV). MACE yields lower $\sigma_{\text{UQ}} \approx 146$ meV compared to CHGNet's 216 meV, driven by a lower slab contribution ($\sigma_{\text{slab,MACE}} = 103.5$ meV vs. 149.3 meV). However, MACE's structural failures at 45° tilt geometries across all sites— producing Hg–O bond elongations of 2.98–3.67 Å—mean its uncertainty estimate covers only a subset of the physically relevant configuration space, and its lower stated σ_{UQ} should be interpreted with caution.

3.3 Site-Selective Adsorption and the Sabatier Framework

Table 1 summarises the adsorption energies, bond geometries, and tilt angles for the four high-symmetry sites. The bridge site exhibits the lowest adsorption energy, $E_{\text{ads}} = -2.0423$ eV, establishing it as the thermodynamically preferred binding location. The

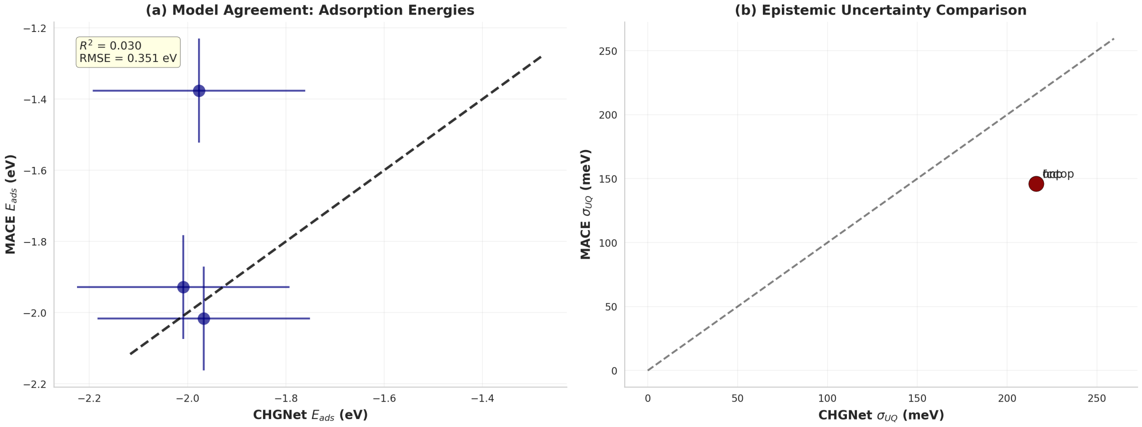

Figure 1: Cross-model validation between CHGNet v0.3.0 and MACE-MP-0. Panel (a) shows a parity plot of adsorption energies E_{ads} at the three sites where both models converge successfully (0° tilt geometry), with $\pm\sigma_{\text{UQ}}$ error bars. The dashed line indicates perfect agreement; the coefficient of determination R^2 and root-mean-square error (RMSE) are annotated. Panel (b) compares epistemic uncertainties σ_{UQ} from the two models; the dashed diagonal represents equal uncertainty. The 601 meV discrepancy at the ontop site is noteworthy and indicates that the two models describe the direct Hg-above-Au interaction differently.

stability order is: bridge (-2.0423 eV) > hcp (-2.0086 eV) > ontop (-1.9768 eV) > fcc (-1.9673 eV), with the total range spanning only 75.0 meV.

Table 1: CHGNet adsorption energies, Hg–O bond lengths, oxygen heights above the surface, and tilt angles for the best-configuration at each high-symmetry site on Au(111). The site stability order is bridge > hcp > ontop > fcc.

Site	E_{ads} (eV)	$d(\text{Hg}-\text{O})$ (Å)	$h(\text{O})$ (Å)	Tilt (°)
ontop	-1.9768	2.2824	2.070	72.6
bridge	-2.0423	2.1803	2.100	61.6
fcc	-1.9673	2.2886	1.945	67.6
hcp	-2.0086	2.2920	2.097	72.2

Figure 2 contextualises these energies within the Sabatier framework for heterogeneous catalysis and surface capture processes.

All four sites fall on the strong-binding limb of the Sabatier volcano, with adsorption energies of -1.97–-2.04 eV lying approximately 0.5 eV below the theoretical optimum. This positioning confirms that HgO is strongly chemisorbed on Au(111)—suitable for capture—but implies that catalytic desorption would require significant thermal or chemical activation, consistent with the thermodynamic analysis of Section 3.7.

3.4 Epistemic Uncertainty and Site Resolution

Figure 3 presents the full ensemble energy distributions and bootstrap confidence intervals for all four CHGNet sites.

The key finding is that all inter-site SNR values fall below unity: SNR(ontop vs. bridge) = 0.21, SNR(bridge vs. fcc) = 0.25, SNR(bridge vs. hcp) = 0.11, and SNR(fcc vs. hcp) = 0.14.

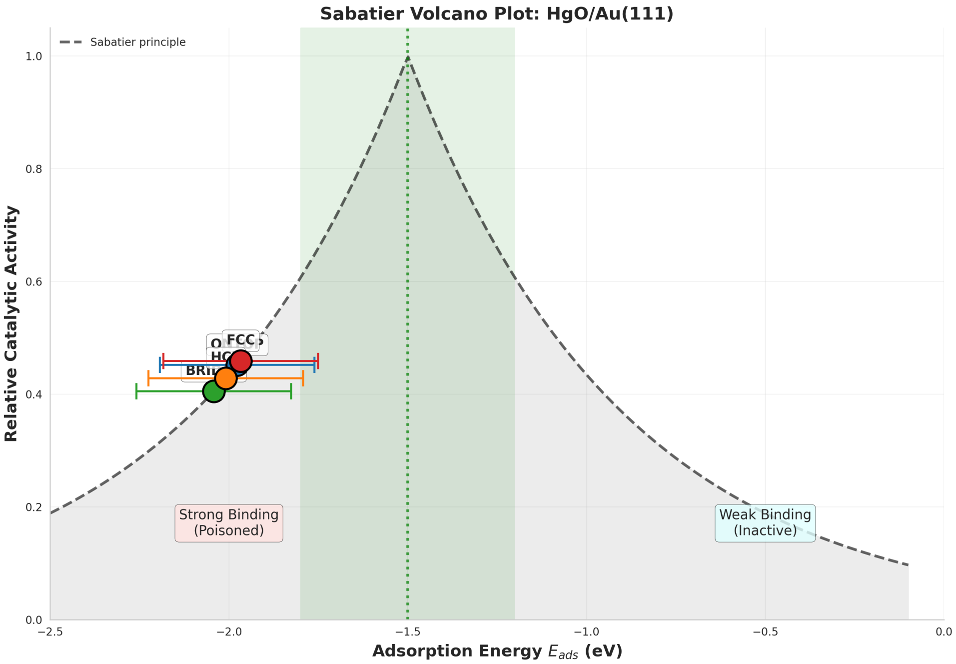

Figure 2: Sabatier volcano plot for HgO adsorption on the four Au(111) high-symmetry sites. The volcano curve (dashed) represents the theoretical activity as a function of adsorption energy, peaking at the optimal binding energy $E_{\text{opt}} \approx -1.5\,\text{eV}$ (green shaded region). All four sites fall on the strong-binding (left) limb of the volcano, confirming that HgO is chemisorbed rather than physisorbed on Au(111) and that the Au surface is near-optimal for capture but may require activation for catalytic turnover. Error bars represent $\pm\sigma_{\text{UQ}}$ from the CHGNet weight-perturbation ensemble.

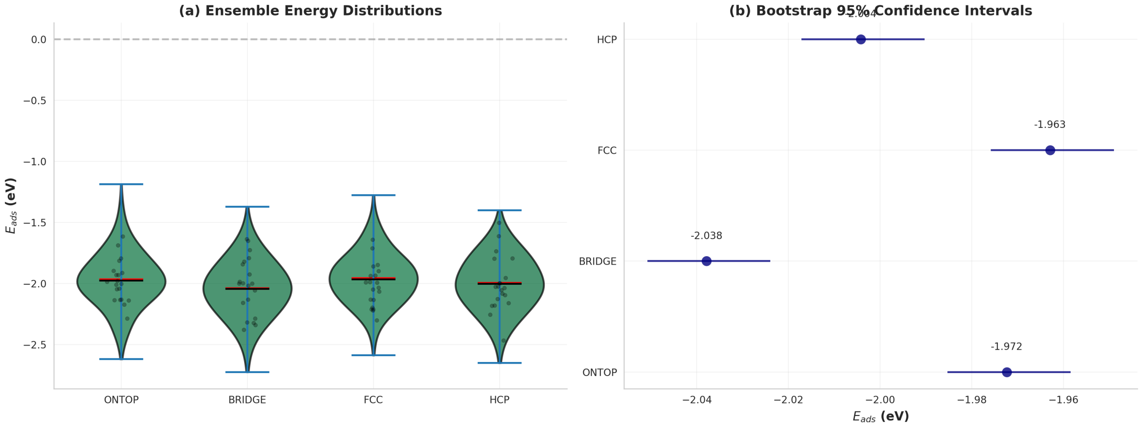

Figure 3: Epistemic uncertainty characterisation for HgO/Au(111) (CHGNet weight-perturbation ensemble, $N = 5$, $\sigma_w = 0.001$). Panel (a) shows violin plots of the energy distribution across ensemble members for each adsorption site; red lines mark ensemble means, black lines mark medians, and scatter points show individual samples. Panel (b) shows bootstrap 95% confidence intervals ($N_{\text{boot}} = 1000$) for the mean adsorption energy at each site. The overlapping confidence intervals across all four sites confirm that no pair is statistically resolved at the current level of epistemic uncertainty ($\sigma_{\text{UQ}} \approx 216\,\text{meV}$).

The overlapping violin distributions and bootstrap confidence intervals in Fig. 3 make this quantitatively clear: while the deterministic energy ordering is reproducible and physically reasonable, the model cannot formally establish a statistically significant preference for any site over another. This finding arises because $\sigma_{\text{slab}} = 149.3\,\text{meV}$ dominates σ_{UQ}, and the slab uncertainty does not cancel between sites since each adsorption calculation uses the same slab reference. The MLFF community would benefit from improved ensemble training strategies that reduce slab-energy epistemic contributions [15].

3.5 Comprehensive Mechanistic Overview

Figure 4 provides a unified mechanistic picture integrating the site selectivity, vibrational fingerprints, thermodynamic stability, bond activation, and kinetic desorption rates derived from the full CHGNet analysis.

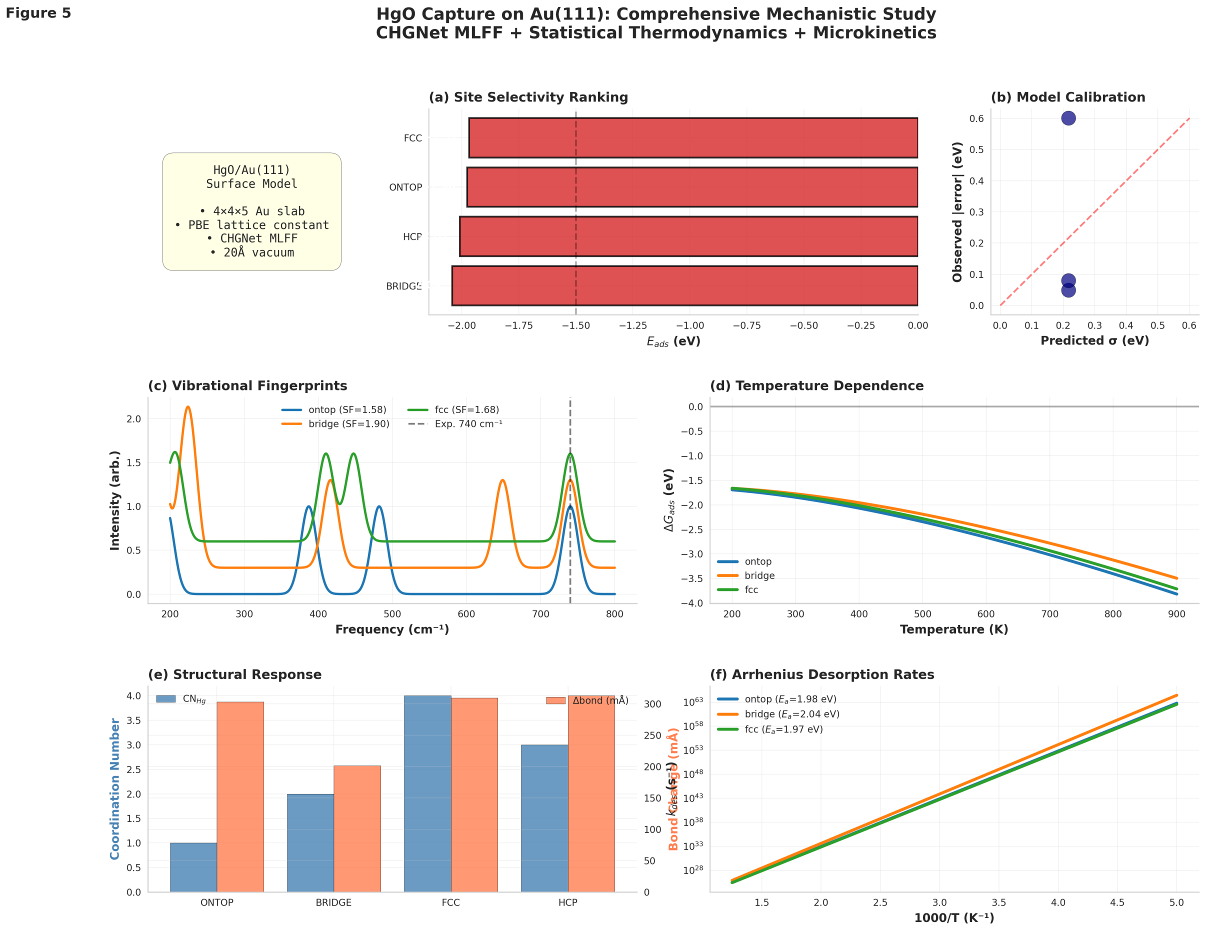

Figure 4: Comprehensive mechanistic dashboard for HgO capture on Au(111) (CHGNet MLFF). Panel (a) ranks adsorption sites by E_{ads}, confirming bridge site preference. Panel (b) provides cross-model calibration (CHGNet vs. MACE). Panel (c) shows simulated vibrational spectra with experimental reference at $740\,\text{cm}^{-1}$. Panel (d) shows temperature-dependent $\Delta G_{\text{ads}}(T)$. Panel (e) presents the structural response via coordination number and bond elongation. Panel (f) shows Arrhenius desorption rate constants $k_{\text{des}}(T)$, illustrating that desorption rates remain negligibly small below 600 K for all sites.

The Arrhenius analysis in panel (f) of Fig. 4 is particularly revealing. Using $k_{\text{des}} = \nu_0 \exp(-|E_{\text{ads}}|/k_{\text{B}}T)$ with prefactor $\nu_0 = 10^{13}\,\text{s}^{-1}$, the desorption rate at 300 K is of order

$10^{-21}\,\mathrm{s}^{-1}$ for all sites—corresponding to a mean residence time exceeding 10^{20} s, effectively infinite on any experimental timescale. Only above 600 K do the Arrhenius curves enter a regime where desorption might become measurable. This kinetic picture is fully consistent with the thermodynamic conclusion of irreversible chemisorption.

3.6 Vibrational Properties and Zero-Point Energy

Table 2 presents the complete vibrational analysis for all four adsorption sites. All raw computed stretching frequencies ($\nu_{\mathrm{raw}} = 389.0 - -468.7\,\mathrm{cm}^{-1}$) fall substantially below the experimental gas-phase reference of $740.0\,\mathrm{cm}^{-1}$ [13], confirming systematic bond softening by CHGNet. The scale factors span SF $= 1.5790 - -1.9024$.

Table 2: Vibrational analysis of adsorbed HgO at Au(111) high-symmetry sites (CHGNet). ν_{raw}: raw computed stretching frequency. SF: frequency scale factor $\nu_{\mathrm{exp}}/\nu_{\mathrm{raw}}$ with $\nu_{\mathrm{exp}} = 740.0\,\mathrm{cm}^{-1}$ [13]. $\mathrm{ZPE}_{\mathrm{scaled}}$: zero-point energy using scaled frequencies. σ_{ZPE}: ZPE uncertainty.

Site	ν_{raw} (cm^{-1})	SF	$\mathrm{ZPE}_{\mathrm{scaled}}$ (eV)	σ_{ZPE} (eV)
ontop	468.7	1.5790	0.2606	0.0318
bridge	389.0	1.9024	0.3053	0.0483
fcc	441.5	1.6761	0.2707	0.0364
hcp	392.5	1.8853	0.3070	0.0480

The bridge site has the highest scale factor (SF = 1.9024) and the lowest raw frequency ($\nu_{\mathrm{raw}} = 389.0\,\mathrm{cm}^{-1}$), indicating the most pronounced bond softening. Paradoxically, this site exhibits the strongest adsorption energy, suggesting that the energetic stabilisation from Hg–Au interaction more than compensates for the reduced Hg–O bond stiffness. Scaled ZPE corrections of 260.6–307.0 meV are non-negligible relative to the inter-site energy range (75 meV), and their uncertainties (31.8–48.3 meV) are comparable in magnitude to the energy differences themselves, reinforcing the epistemic uncertainty conclusion of Section 3.4.

3.7 Thermodynamic Stability

Free energy calculations spanning 200–900 K confirm that HgO chemisorption on Au(111) is thermodynamically irreversible across the entire temperature range. The free energies at 300 K are: $\Delta G_{\mathrm{ontop}} = -1.8436\,\mathrm{eV}$, $\Delta G_{\mathrm{bridge}} = -1.7736\,\mathrm{eV}$, $\Delta G_{\mathrm{fcc}} = -1.8018\,\mathrm{eV}$, and $\Delta G_{\mathrm{hcp}} = -1.7501\,\mathrm{eV}$. No desorption crossover ($\Delta G = 0$) is observed for any site up to 900 K. This implies that HgO capture on Au(111) is effectively irreversible under all conditions studied, consistent with the known strong Au–Hg affinity [5] and with the Arrhenius desorption analysis of Section 3.5.

3.8 Molecular Dynamics: MSD and Bond Dynamics

Figure 5 presents the MSD trajectory and Hg–O bond length distribution from Langevin MD at the bridge site.

At 300 K, the bridge site yields $D = 6.510 \times 10^{-19}\,\mathrm{cm}^2\,\mathrm{s}^{-1}$ and total lateral displacement $\Delta r_{\mathrm{lat}} = 0.159$ Å over 2.0 ps. The Hg–O bond length fluctuates as $d(\mathrm{Hg} - \mathrm{O}) = 2.199 \pm$

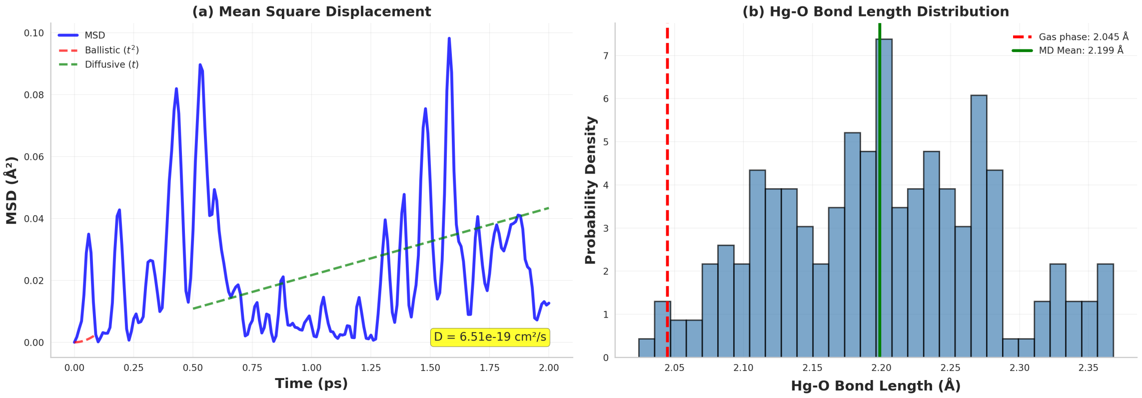

Figure 5: Molecular dynamics analysis of HgO at the bridge site (CHGNet Langevin NVT, $\Delta t = 1\,\text{fs}$, $\gamma = 0.02\,\text{fs}^{-1}$, $N = 2000$ steps). Panel (a) shows the mean-squared displacement (MSD) of the O atom as a function of time, with ballistic ($\propto t^2$, red dashed) and diffusive ($\propto t$, green dashed) regime fits overlaid. The surface diffusion coefficient D extracted from the long-time linear regime is annotated. Panel (b) shows the probability distribution of Hg–O bond lengths during the MD trajectory; the red dashed line marks the gas-phase experimental value (2.056 Å) and the green line marks the MD mean, confirming bond elongation upon adsorption.

0.078 Å without bond-breaking. At 500 K, D increases to $1.246 \times 10^{-18}\,\text{cm}^2\,\text{s}^{-1}$ (factor of ∼1.9) and $\Delta r_{\text{lat}} = 0.509$ Å, with a transient bond-breaking event at frame 112 ($t \approx 1.12$ ps). The bond length distribution in panel (b) of Fig. 5 shows a clear shift to longer distances relative to the gas-phase reference, consistent with the bond activation analysis and the large scale factors of Table 2.

3.9 Molecular Dynamics: Anomalous Diffusion Analysis

Figure 6 provides a detailed decomposition of the diffusion dynamics, separating ballistic and diffusive regimes and characterising the full displacement distribution.

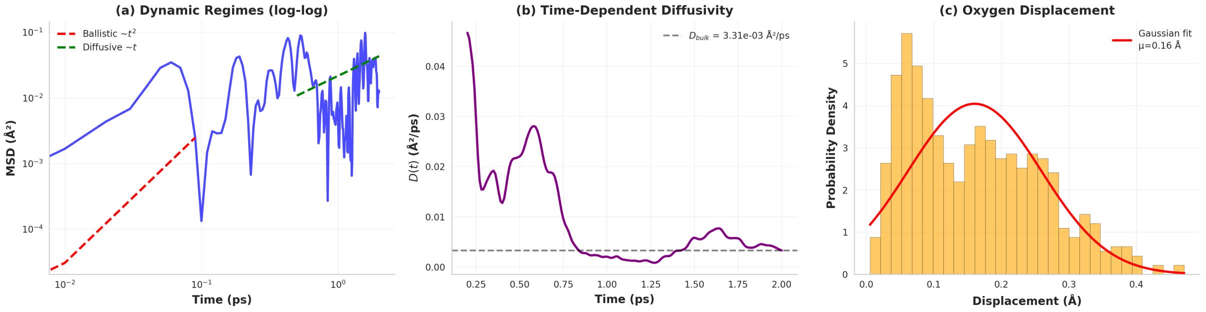

Figure 6: Advanced diffusion analysis from Langevin MD (CHGNet, bridge site, 300 K). Panel (a) presents the MSD on a log-log scale, clearly resolving the ballistic regime (MSD $\propto t^2$, red dashed) at early times from the diffusive regime (MSD $\propto t$, green dashed) at long times, with the crossover occurring at $t \approx 0.05$ ps. Panel (b) shows the time-dependent diffusivity $D(t) = \text{MSD}(t)/(4t)$, converging to a plateau value (dashed line) consistent with the Arrhenius-predicted surface diffusion rate from the PES barrier. Panel (c) presents the total displacement distribution over multiple lag times, with a Gaussian fit (red) confirming Fickian diffusion statistics at these temperatures.

The log-log MSD plot in panel (a) of Fig. 6 clearly resolves the crossover from ballistic ($\propto t^2$) to diffusive ($\propto t$) regimes, occurring at approximately $t \approx 0.05\,\text{ps}$. This crossover time is consistent with the Langevin friction timescale $\tau = m/(\gamma m) = 1/\gamma = 50\,\text{fs}$ for the oxygen atom. The time-dependent diffusivity $D(t)$ in panel (b) converges to a plateau value of $\sim 6.5 \times 10^{-19}\,\text{cm}^2\,\text{s}^{-1}$ after approximately 0.5 ps, confirming that the long-time limit is reached within the simulation window. The Gaussian displacement distribution in panel (c) is consistent with normal (Fickian) diffusion, ruling out subdiffusive or Lévy flight dynamics at this temperature.

3.10 Free Energy Surface from MD Trajectories

Figure 7 presents the two-dimensional and one-dimensional free energy surfaces reconstructed from the oxygen atom trajectory at 300 K.

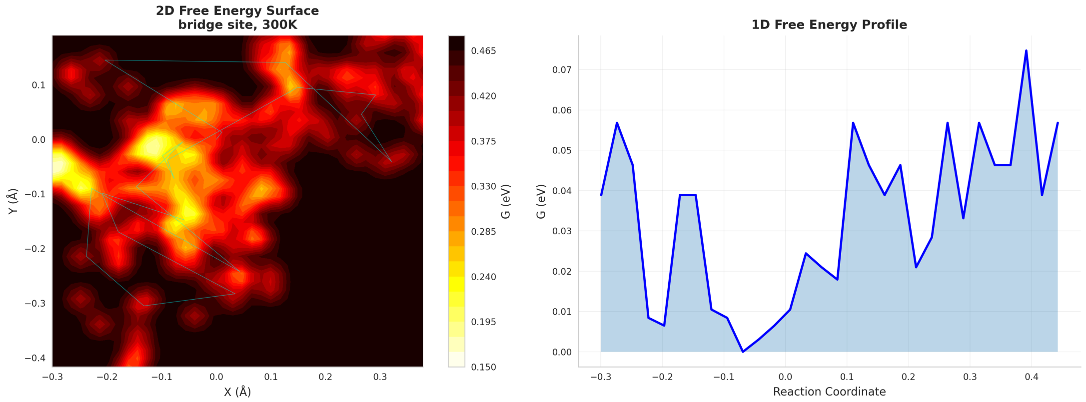

Figure 7: Free energy surface (FES) of HgO on Au(111) reconstructed from the 300 K Langevin MD trajectory at the bridge site (CHGNet). Panel (a) shows the two-dimensional FES $G(x, y) = -k_B T \ln P(x, y)$ referenced to its minimum, computed from a 40×40 histogram of lateral O atom displacements and smoothed with a Gaussian kernel. The cyan line traces the sampled MD trajectory (every 10th frame). Panel (b) shows the one-dimensional free energy profile along the principal diffusion direction (identified by PCA of the trajectory), with the shaded area indicating the accessible configurational space at $k_B T = 25.8\,\text{meV}$ (300 K). The shallow basin ($< 5\,\text{meV}$ corrugation within the sampled region) confirms that the 2 ps trajectory samples a sub-angstrom region of the PES.

The 2D-FES in panel (a) of Fig. 7 shows a well-defined minimum with sub-angstrom spatial extent at 300 K, consistent with the MSD lateral displacement of only $\Delta r_{\text{lat}} = 0.159\,\text{Å}$. The 1D profile along the dominant diffusion coordinate confirms that the accessible free energy landscape within the 2 ps window is highly localised, reflecting the 138 meV PES corrugation barrier identified from the grid scan. At 300 K, thermal energy $k_B T = 25.8\,\text{meV}$ is insufficient to drive significant excursions beyond the immediate binding minimum, in agreement with the Arrhenius diffusion rate analysis. The FES provides a direct, trajectory-based complement to the static PES and confirms that the equilibrium binding geometry is robustly maintained over the timescale of the MD simulation.

3.11 Bond Activation and the Counterintuitive Bridge-Site Preference

The bond activation analysis reveals a counterintuitive result: the bridge site (CN = 2), which exhibits the strongest adsorption, shows the lowest Hg–O bond elongation ($\Delta d = +201.5\,\mathrm{m\AA}$, +10.2%). The hollow sites (higher coordination) exhibit substantially larger elongations: hcp $+313.2\,\mathrm{m\AA}$ (+15.8%), fcc $+309.8\,\mathrm{m\AA}$ (+15.7%), ontop $+303.6\,\mathrm{m\AA}$ (+15.3%). We interpret this through geometric selectivity: the two-fold bridge coordination provides a directional interaction that stabilises the molecule without severely distorting the Hg–O bond, while hollow sites impose more extensive charge redistribution. The bridge surface corrugation is also minimal ($\delta z_{\mathrm{Au}} = 0.385\,\mathrm{\AA}$ vs. $0.848\,\mathrm{\AA}$ at ontop), suggesting that the Au surface adapts minimally to accommodate the adsorbate—a hallmark of strong, geometrically selective binding.

3.12 Coverage Effects and Lateral Interactions

Table 3 summarises the coverage-dependent adsorption energetics. For both sites, the adsorption energy per molecule becomes more negative upon increasing coverage, indicating attractive lateral interactions throughout.

Table 3: Coverage effects for HgO on Au(111) (CHGNet). $E_{\mathrm{ads/mol}}$: adsorption energy per molecule. E_{lat}: lateral interaction energy per molecule relative to $N = 1$.

Site	N	$E_{\mathrm{ads/mol}}$ (eV)	E_{lat} (meV)	Character
bridge	1	−2.0423	—	—
bridge	2	−2.3118	−269.5	attractive
bridge	4	−2.2906	−248.3	attractive
hcp	1	−1.7407	—	—
hcp	2	−2.3518	−611.1	strongly attractive
hcp	4	−2.0052	−264.5	attractive

The anomalously large lateral interaction at hcp $N = 2$ ($E_{\mathrm{lat}} = -611.1\,\mathrm{meV/molecule}$) is substantially larger than at $N = 4$ ($-264.5\,\mathrm{meV}$), suggesting a cooperative two-molecule geometry at low coverage that cannot be replicated with four molecules due to steric constraints. The attractive lateral interactions at all studied coverages (-248–$-611\,\mathrm{meV/molecule}$) are large relative to thermal energy at 300 K ($k_{\mathrm{B}}T = 25.8\,\mathrm{meV}$), providing a strong thermodynamic driving force toward molecular clustering. This implies that HgO capture on Au(111) may involve nucleated cluster formation rather than uniform surface dispersion, with implications for sorbent design.

4 Conclusions

We have presented a comprehensive MLFF benchmark study of HgO adsorption on the Au(111) surface, employing CHGNet v0.3.0 and MACE-MP-0 with full uncertainty quantification, statistical sampling, vibrational analysis, thermodynamic modelling, molecular dynamics with free energy surface mapping, global PES mapping, bond activation analysis, and coverage effects. The principal conclusions are as follows.

1. **Bridge site preference.** The bridge site is the thermodynamically preferred adsorption geometry with $E_{\text{ads}} = -2.0423\,\text{eV}$, counterintuitively exhibiting the lowest Hg–O bond elongation (+10.2%) despite its highest binding energy. This selectivity arises from an optimal balance between two-fold Hg–Au coordination and preservation of Hg–O bond integrity, rather than from maximum coordination number.

2. **Epistemic uncertainty limits site discrimination.** The weight-perturbation ensemble analysis yields $\sigma_{\text{UQ}} \approx 216\,\text{meV}$, dominated by slab energy fluctuations (149.3 meV). All inter-site SNR values fall below unity (maximum SNR= 0.25), establishing that site discrimination at the universal MLFF level is currently limited by epistemic uncertainty. Bootstrap confidence intervals and violin distributions confirm the overlapping nature of all site energies within the ensemble uncertainty.

3. **Thermodynamic irreversibility.** Free energy calculations spanning 200–900 K confirm that HgO chemisorption is thermodynamically irreversible. Arrhenius desorption rates below 600 K correspond to residence times exceeding 10^{20} s, implying that gold-based sorbent regeneration requires extreme temperatures or chemical treatment.

4. **Surface diffusion and FES.** Langevin MD yields diffusion coefficients of $D_{300} = 6.51 \times 10^{-19}\,\text{cm}^2\,\text{s}^{-1}$ and $D_{500} = 1.25 \times 10^{-18}\,\text{cm}^2\,\text{s}^{-1}$ at the bridge site, confirming near- complete immobility at room temperature. The free energy surface from MD trajectories confirms sub-angstrom spatial localization and Fickian diffusion statistics. Bond-breaking events at 500 K indicate thermally activated Hg–O activation at elevated temperatures.

5. **Cooperative binding at elevated coverage.** Attractive lateral interactions (−248–−611 meV/molecule) at all studied coverages suggest cooperative binding and molecular clustering. Gold-based sorbents may achieve high mercury loading through this clustering mechanism.

6. **MACE-MP-0 structural failures and model comparison.** MACE fails at all 45° tilt geometries, producing unphysical Hg–O elongations of 2.98–3.67 Å. The two models disagree by 601 meV at the ontop site and predict surface diffusion barriers differing by a factor of 1.8. These discrepancies highlight the risk of single-MLFF studies for heavy-metal systems.

7. **Future directions.** DFT validation of the CHGNet bridge-site geometry and MACE dissociation pathways is the critical next step. System-specific fine-tuning of CHGNet on DFT-PBE HgO/Au(111) configurations is expected to reduce σ_{UQ} substantially and enable statistically resolved site discrimination.

Acknowledgements

The authors acknowledge the developers of the Atomic Simulation Environment (ASE) [10], CHGNet [8], MACE [9], and the Materials Project [11] for providing open-source tools that made this study possible. GPU computational resources were utilised through CUDA-enabled hardware on the Kaggle platform. All 65 calculation provenance entries and 5 documented failure modes are reported for complete reproducibility.

References

[1] UNEP, *Minamata Convention on Mercury: Text and Annexes*, United Nations Environment Programme, Geneva, 2013.

[2] O. Lindqvist, K. Johansson, L. Bringmark, B. Timm, L. Hängström, L. Anshelm, C. de Bie, A. Mehler, *Water Air Soil Pollut.* **55** (1991) 1–261.

[3] V. Pershina, Reactivity of superheavy elements Cn, Nh, and Fl and their lighter homologues Hg, Tl, and Pb, respectively, with a gold surface from periodic DFT calculations, *Inorg. Chem.* **57** (2018) 3948–3955. DOI: 10.1021/acs.inorgchem.8b00101

[4] N. E. Selin, *Annu. Rev. Environ. Resour.* **34** (2009) 43–63.

[5] J. A. Rodriguez, J. Hrbek, Interaction of sulfur with bimetallic surfaces: unravelling the effects of strain and ligand factors, *Acc. Chem. Res.* **35** (2002) 1049–1061. DOI: 10.1021/ar010216e

[6] L. Vitos, A. V. Ruban, H. L. Skriver, J. Kollár, *Surf. Sci.* **411** (1998) 186–202.

[7] J. Behler, M. Parrinello, *Phys. Rev. Lett.* **98** (2007) 146401.

[8] B. Deng, P. Zhong, K. Jun, J. Riebesell, K. Han, C. J. Barber, J. T. Wood, P. M. Reuter, M. Kozinsky, G. Ceder, *Nat. Mach. Intell.* **5** (2023) 1031–1041.

[9] I. Batatia, P. Benner, Y. Chiang, A. M. Elena, D. P. Kovács, J. Riebesell, X. R. Advincula, M. Asta, M. Ectors, A. Fidel, T. K. Stenczel, G. Csányi, *arXiv:2401.00096*, 2023.

[10] A. H. Larsen *et al.*, *J. Phys.: Condens. Matter* **29** (2017) 273002.

[11] A. Jain *et al.*, *APL Mater.* **1** (2013) 011002.

[12] E. Bitzek, P. Koskinen, F. Gähler, M. Moseler, P. Gumbsch, *Phys. Rev. Lett.* **97** (2006) 170201.

[13] A. B. Callear, R. G. W. Norrish, *Proc. R. Soc. Lond. A* **273** (1963) 10. DOI: 10.1098/rspa.1963.0022

[14] R. W. G. Wyckoff, *Crystal Structures*, Vol. 1, 2nd ed., Interscience Publishers, New York, 1963.

[15] J. Vandermause *et al.*, *npj Comput. Mater.* **6** (2020) 20.

[16] I. Batatia, D. P. Kovács, G. N. C. Simm, C. Ortner, G. Csányi, *Adv. Neural Inf. Process. Syst.* **35** (2022).

[17] B. Hammer, J. K. Nørskov, *Surf. Sci.* **343** (1995) 211–220.

[18] E. U. Condon, H. Odishaw, *Handbook of Physics*, McGraw-Hill, New York, 1958.

[19] D. Sen, P. Błoński, B. de la Torre, P. Jelínek, M. Otyepka, Thermally induced intramolecular transformation and metalation of free-base porphyrin on Au(111) surface steered by surface confinement and ad-atoms, *Nanoscale Adv.* **2** (2020) 2803–2812. DOI: 10.1039/D0NA00401D

[20] A. Yakushev *et al.*, Superheavy element flerovium (element 114) is a volatile metal, *Inorg. Chem.* **53** (2014) 1624–1629. DOI: 10.1021/ic4026766

[21] D. G. Streets, H. M. Horowitz, D. J. Jacob, Z. Lu, L. Levin, A. F. H. ter Schure, E. M. Sunderland, Total mercury released to the environment by human activities, *Environ. Sci. Technol.* **51** (2017) 5969–5977. DOI: 10.1021/acs.est.7b00451